Realization and Simulation of High-Aspect-Ratio Micro/Nanostructures by Proton Beam Writing

Evangelos VALAMONTES[1,2], Margarita CHATZICHRISTIDI[3], Nikolaos TSIKRIKAS[3],
Dimitrios GOUSTOURIDIS[3], Ioannis RAPTIS[3*], Constantinos POTIRIADIS[4],
Jeroen Anton VAN KAN[5], and Frank WATT[6]

[1]*Department of Telecommunications, University of Peloponnese, GR-22100 Tripoli, Greece*
[2]*Department of Electronics, TEI of Athens, Aegaleo 12210, Greece*
[3]*Institute of Microelectronics, NCSR "Demokritos", Athens 15310, Greece*
[4]*Greek Atomic Energy Commission, Agia Paraskevi, Attiki 15310, Greece*
[5]*Engineering Science Programme, CIBA, Physics Department, National University of Singapore, Singapore*
[6]*Centre for Ion Beam Applications, Physics Department, National University of Singapore, Singapore*

Among the patterning technologies proposed and applied for the realization of high-aspect-ratio structures in the micro- and nanoscale, proton beam writing (PBW) is considered to be a valuable tool for maskless patterning of such structures owing to the unique ability of protons to maintain a straight path over long distances. In this work, the PBW capabilities are demonstrated through simulation results of fine structures in resist films. These results prove the capability of PBW to produce very tall structures with almost vertical sidewalls, with the aspect ratio limited practically only by the resist performance and the beam diameter provided. The performance of PBW is explored and proved through the patterning of an aqueous base developable negative chemically amplified resist (TADEP, thick aqueous base developable epoxy based resist). By employing PBW on a 2.0-μm-thick TADEP, patterns with 110 nm linewidth and an aspect ratio of 18 were resolved.
[DOI: 10.1143/JJAP.47.8600]

1. Introduction

The mainstream high-resolution direct-write (maskless) lithography technologies are based on charged particles such as electron beam lithography (EBL) and focused ion beam lithography (FIBL). These technologies provide high-resolution patterning in very thin films. However, there are technological fields where there is a requirement for very tall and fine structures, i.e., structures with high-aspect-ratio characteristics. Originally in this area (high-aspect-ratio micromachining, HARM), the target was the patterning of very thick films and several technologies were developed, the most successful among them being XR-LIGA (X-ray lithographie Galvanoformung Abformung)[1] and UV-LIGA (ultra violet lithographie Galvanoformung Abformung).[2] In several cases, the lateral critical dimension lies in the sub-100 nm range (high-aspect-ratio nanomachining, HARN). However, in both LIGA technologies, a mask is required which in the case of XR-LIGA is expensive. As the devices continue to shrink, the need for high-aspect-ratio structures with submicron critical dimensions increases and UV-LIGA has severe limitations. For application in these devices, EBL and FIBL are inadequate and a new maskless lithography technology with resolution capabilities in the 100 nm regime is required. In this area, a maskless patterning technology based on proton beams focused in the sub-100 nm beam diameter range (proton beam writing, PBW)[3,4] has recently emerged. However, in XR-LIGA, the proximity effect due to forward scattering is not an issue, which is a significant advantage over PBW for thick resist patterning. In addition, the maximum resist thickness that can be exposed by PBW (2 MeV) is limited to a few tens of μm, whereas this is not an issue for XR-LIGA. However, since PBW is a maskless technology, it is promising for applications such as fabrication of a number of small parts and in research and development.

The principle of operation of PBW, such as in terms of interaction with the matter and writing strategy, is very close to that of e-beam lithography. In this work, the advantages of PBW for the fabrication of high resolution structures are explored and presented through both simulation and experimental results.

For the simulation of PBW, a complete model of proton energy transfer from a proton beam to a photoresist has been developed. To build a complete model of proton energy loss, two issues have to be addressed: the first is the proton scattering process in the materials (propagation) and the second is the energy transfer mechanism from protons to the photoresist (deposition). To understand the proton scattering process, the continuous slowing down approximation (CSDA) has been used in our Monte Carlo simulations.

In addition to the simulation, high resolution and high aspect ratio results from the application of PBW to a negative chemically amplified resist are presented.

2. Simulation Modules and Materials

2.1 Simulation strategy

For the PBW simulation several modules (exposure, thermal processing, development) should be coupled in a software tool. In the present case, the following simulation strategy is shown in Fig. 1. As the principle of operation of PBW has many characteristics in common with EBL, the simulation strategy for PBW follows that for EBL.[5] The first simulation module is used to calculate the energy loss distribution in the resist film and the substrate due to a point proton beam irradiation, the second is used to perform the convolution of the energy deposition with the proton beam profile (Gaussian in this case) and the third is used to perform the convolution with the layout of interest. Then, in the case of chemically amplified resists, a simulation of the

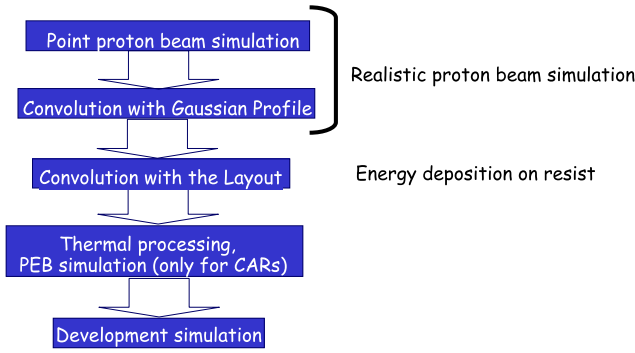*E-mail address: raptis@imel.demokritos.gr

Fig. 1.   (Color online) Proton beam simulation flow chart.

PEB follows. The last simulation module is the dissolution, which in this work is a simple absorbed energy threshold. All modules except for the first one are identical to the EBL ones; however, it should be noted that the films used in the PBW are considerably thicker than those used in EBL, leading to increased simulation times. To simplify the simulation study of PBW, poly(methyl methacrylate) (PMMA) films are considered in this study.

2.2   Simulation modules
2.2.1   Analytical evaluation of the scattering angle

We introduce the dimensionless "reduced" energy

$$\varepsilon = \frac{aE_C}{Z_1 Z_2 e^2}, \tag{1}$$

where Z_1 and Z_2 are the proton and target atomic numbers, respectively, e is the electronic charge, α is the screening length, and $E_C = E/(1 + M_1/M_2)$ is the energy available in the center of mass system. We have chosen to use the universal screening length given as

$$a = \frac{0.8853 a_0}{Z_1^{0.23} + Z_2^{0.23}}, \tag{2}$$

where $a_0 = 0.52917\,\text{Å}$ is the Bohr radius. We define $B = p/a$, expressing the impact parameter p in units of the screening length.

The formalism adopted for simulating proton propagation is that of TRIM/STRIM.[6,7] Although this formalism for nuclear scattering based on the universal potential has built-in validity for large values of ε, we have decided, for the sake of computer efficiency, to base the calculations on the Coulomb potential for $\varepsilon > 10$. For the Coulomb potential, $\sin^2(\theta/2)$ is simply related to ε and B by the following expression:

$$\sin^2\left(\frac{\theta}{2}\right) = \frac{1}{1 + (2\varepsilon B)^2}, \tag{3}$$

where θ is the deflection angle in the center of mass system. The use of the Coulomb potential for $\varepsilon > 10$ should affect the results of the calculations only slightly while reducing the computing time.

2.2.2   Angular deflection

The above formalism for nuclear scattering provides the scattering angle ψ in the center of mass system. The scattering angle ψ in the laboratory system is given by the following relation:

$$\psi = \arctan\left[\frac{\sin\theta}{\cos\theta + (M_1/M_2)}\right]. \tag{4}$$

The azimuthal scattering angle φ is randomly selected using the relation:

$$\phi = 2\pi R_n, \tag{5}$$

where R_n is a random number uniformly distributed between 0 and 1.

In actual calculations, the particles are followed with reference to a fixed axis, which is chosen to be normal to the target surface. The angle α, with respect to this axis is determined after each collision. The cosine of this angle, after the ith collision, is given as

$$\cos\alpha_i = \cos\alpha_{i-1}\cos\psi + \sin\alpha_{i-1}\sin\psi\cos\phi. \tag{6}$$

The angles with respect to the other Cartesian coordinates (lateral directions) are determined for following the particle trajectories in a three-dimensional space and are given by the following relations:

$$\sin(\phi_i - \phi_{i-1}) = \frac{\sin\psi\sin\phi}{\sin\alpha_i}, \tag{7a}$$

and

$$\cos(\phi_i - \phi_{i-1}) = \frac{\cos\psi - \cos\alpha_i\cos\alpha_{i-1}}{\sin\alpha_i\sin\alpha_{i-1}}. \tag{7b}$$

The new scattering coordinates were determined from

$$\begin{pmatrix} x_{i+1} \\ y_{i+1} \\ z_{i+1} \end{pmatrix} = \begin{pmatrix} x_i \\ y_i \\ z_i \end{pmatrix} + L_i \begin{pmatrix} \sin a_i \cos\phi_i \\ \sin a_i \sin\phi_i \\ \cos a_i \end{pmatrix}.$$

2.2.3   Distance between collisions and impact parameter selection

At high energies, $\varepsilon \gg 10$, only a few of the many encounters in the target cause significant deflections from the straight path of flight. Even over distances L, which is large compared with the interatomic distance in a solid, a noticeable deflection ($\psi > 1°$) is a rare event, associated with a very small impact parameter. Therefore, the program is set up to select the smallest impact parameter that occurs over the path length L, and neglect the other collisions with larger impact parameters and smaller deflection angles.

The smallest impact parameter over the path length L is found in the following way. The probability $W_1(p)\delta p$ for finding a target atom at a radial distance between p and $p + \delta p$ is

$$W_1(p)\delta p = NL2\pi p\delta p,$$

where N is the atomic density of the target. The probability for not finding another atom closer than p is

$$W_2(p) = e^{-NL\pi p^2}.$$

Hence, the probability for finding the closest target atom between p and $p + \delta p$ (provided no other atom is closer) becomes the product of

$$W(p)\delta p = W_2(p)W_1(p)\delta p = e^{-NL\pi p^2}NL2\pi p\delta p. \tag{8}$$

This probability distribution leads to the impact parameter determination

$$p = \left(-\frac{\ln R_n}{\pi N L}\right)^{1/2}, \qquad (9)$$

from random numbers R_n, which are evenly distributed between 0 and 1.

For high energies, the length L is chosen[7]

$$L = \frac{0.02[1 + (M_1/M_2)]^2}{4\pi a^2 N} \cdot \frac{\varepsilon^2 + 0.1\varepsilon^{1.38}}{\ln(1 + \varepsilon)}. \qquad (10)$$

By choosing the free flight path in this way, one is assured that $L(\varepsilon)$ is always short compared with the mean distance between large angle deflections ($\psi > 10^0$). Therefore, it does not matter where such a deflection occurs within each L-interval, which justifies the assumption of placing the collision at each interval's end. In the high-energy region, a second independent check is performed on the path length L to ensure that the electronic energy loss does not exceed 5% of the ion energy. In cases where this happens, the path length L is reduced accordingly.

For low energies, the approximate mean atomic separation $N^{-1/3}$ is used for L. In this case, the impact parameter has to be chosen according to

$$W(p)\delta p = \begin{cases} 2\pi N^{2/3} p \delta p & \text{for } p < \pi^{-1/2} N^{-1/3}, \\ 0 & \text{for } p > \pi^{-1/2} N^{-1/3}, \end{cases} \qquad (11)$$

since now only one atom is assumed in the volume element of length $N^{-1/3}$ and base area of $N^{-2/3}$. This assumption leads[7] to the determination of the impact parameter

$$p = \left(\frac{R_n}{\pi N^{2/3}}\right)^{1/2}. \qquad (12)$$

2.2.4 Stopping power

The stopping power of a material is defined as the average energy loss per unit path length, which charged particles suffer when traversing the material, as the result of Coulomb interactions with electrons and atomic nuclei. For protons, the predominant contribution to the total stopping power comes from electronic stopping power, $-(dE/dx)_{\text{el}}$, owing to inelastic collisions with electrons. A smaller contribution comes from the nuclear stopping power, $-(dE/dx)_{\text{nuc}}$, due to elastic Coulomb collisions in which recoil energy is imparted to atoms. The nuclear stopping power is important only at very low energies.

In this paper, electronic stopping powers at high energies were calculated on the basis of Bethe's theory with various refinements (shell corrections, corrections for departures from the first Born approximation, and the density effect correction).[8]

The formula for the mass electronic stopping power for a proton can be written in the form

$$-\frac{1}{\rho}\left(\frac{dE}{dx}\right)_{\text{el}} = \frac{4\pi r_e^2 mc^2}{\beta^2} \frac{1}{u} \frac{Z}{A} L(\beta)$$
$$= 0.307075 \frac{1}{\beta^2} \frac{Z}{A} L(\beta) \text{ MeV cm}^2\,\text{g}^{-1}, \qquad (13)$$

where r_e is the classical electron radius, mc^2 is the electron rest energy, u is the atomic mass unit, β is the particle velocity in units of the velocity of light, and Z and A are the atomic number and relative atomic mass of the target atom, respectively. The quantity L is called stopping number and

takes into account the various refinements. It is convenient to express the stopping number as the sum of three terms

$$L(\beta) = L_0(\beta) + L_1(\beta) + L_2(\beta). \qquad (14)$$

The first term is given as

$$L_0(\beta) = \frac{1}{2}\ln\left(\frac{2mc^2\beta^2 W_m}{1 - \beta^2}\right) - \beta^2 - \ln I - \frac{C}{Z} - \frac{\delta}{2}, \qquad (15)$$

where I is the mean excitation energy of the medium, C/Z is the shell correction, and $\delta/2$ the density-effect correction. W_m is the largest possible energy loss in a single collision with a free electron. The terms L_1 (Barkas correction) and L_2 (Bloch correction) take into account departures from the first-order Born approximation, and are important only for low projectile velocities.

At low energies, electronic stopping powers were obtained from experimental data, with heavy reliance on the empirical fitting formulas developed by Andersen and Ziegler.[9] Andersen and Ziegler used as an independent variable not the energy but a scaled energy T_S, which is equal to energy (in keV) divided by M_P/u. The stopping cross section is fitted using (8):

$$\varepsilon = \frac{\varepsilon_{\text{low}} \cdot \varepsilon_{\text{high}}}{\varepsilon_{\text{low}} + \varepsilon_{\text{high}}}, \qquad (16)$$

where

$$\varepsilon_{\text{low}} = A_2 T_S^{0.45},$$

and

$$\varepsilon_{\text{high}} = \frac{A_3}{T_S}\ln\left(1 + \frac{A_4}{T_S} + \frac{A_5}{T_S}\right).$$

For T_S between 1 and 10 keV, where measurements are scarce, we assumed the theoretical result:[8]

$$\varepsilon = A_1 T_S^{0.5}. \qquad (17)$$

Nuclear stopping powers were obtained by calculating the transfer of energy to the recoiling atoms in elastic collisions. The cross section of the elastic scattering by atoms was obtained by a classical trajectory calculation according to the method of Everhart *et al.*[10] The nuclear stopping power is important only at very low energies.

Mean excitation energies for compounds were obtained using Bragg's additivity rule. According to this rule, the mass stopping power for a compound can be approximated using a linear combination of the stopping powers for the atomic constituents:

$$-\frac{1}{\rho}\left(\frac{dE}{dx}\right)_{\text{el}} = -\sum_j w_j \left[\frac{1}{\rho}\left(\frac{dE}{dx}\right)_{\text{el}}\right]_j, \qquad (18)$$

where w_j is the fraction by weight and $-[1/\rho(dE/dx)_{\text{el}}]_j$ is the mass electronic stopping power of the jth constituent. The corresponding relation for the mean excitation energy is

$$\ln I = \left[\sum_j w_j \left(\frac{Z_j}{A_j}\right) \ln I_j\right] \Big/ \left\langle\frac{Z}{A}\right\rangle,$$

where

$$\left\langle\frac{Z}{A}\right\rangle = \sum_j w_j \left(\frac{Z_j}{A_j}\right).$$

2.3 PBW tool

The PBW technology was developed at the Centre for Ion Beam Applications (CIBA) at the National University of Singapore by using a MeV proton beam focused to small spot sizes using a system of strong focusing quadrupole lenses and scanned across a resist. In PBW, the beam is scanned across a resist material in a predetermined pattern, following the direct-writing EBL approach, which is subsequently developed to produce three-dimensional structures. The CIBA setup is capable of producing proton beams with an energy of a few MeV and a diameter in the sub-100 nm range. Details on this particular set-up can be found in ref. 11. In this study, all irradiations were carried out with 2 MeV of energy and with a beam focused to 100×200 nm^2 for the 2-µm-thick film and 200×250 nm^2 for the 12-µm-thick film. The exposure field used in all experiments was 40×40 µm^2 with a beam step size of 10 nm.

2.4 TADEP resist

In this work, TADEP resist is patterned by PBW. TADEP consists of partially hydrogenated poly(hydroxystyrene) (PHPHS), epoxy novolac (EP), and a sulfonium salt as the photoacid generator (PAG), and is capable of providing film thickness of up to 55 µm with one spin coating step. The processing steps are (a) spin coating from a suitable solution, (b) post apply bake (PAB) on a leveled hot plate at 95 °C for a certain time depending on the film thickness, (c) proton beam exposure, (d) post exposure bake (PEB) at 110 °C for a certain time depending on the film thickness, (e) development in TMAH 0.26 N (AZ-726MIF from AZ-EM) for the dissolution of the uncrosslinked areas, and (f) rinsing in deionized H$_2$O. Stripping is performed in acetone in an ultrasonic bath. Detailed information on the resist's chemistry and processing can be found in ref. 12.

3. Results

3.1 Simulation results

By applying the simulation software presented in §2.2, the proton beam interaction with matter for the materials and thicknesses of interest for PBW was explored. In Fig. 2, the energy deposition vs sample depth, due to point proton beam exposure, for 18 µm PMMA film thickness, is illustrated. It is clear that for all PMMA film thicknesses the energy deposition does not depend on the substrate, i.e., there is an absence of backscattering contribution, which is a major resolution-limiting factor in the case of electron beam lithography. From this figure, it is clear that even for 18 µm resist thickness the energy deposition is not markelly different from the energy deposited on the resist's surface (the calculated increase is 17%). This limited dependence of the energy deposition on the resist depth is one of the advantages of the PBW over the EBL for the patterning of thick films. The highest percentage of the initial proton beam energy is deposited very close to the proton's range, which in the case of the 2 MeV, used in this present study, is approximately 60 µm. In the inset of Fig. 2, the proton trajectories for a 10 µm polymer film on bulk Si substrate are shown, where the limited broadening in the polymer film is obvious.

In Fig. 3 the energy deposition vs lateral dimension for various resist depths is shown. It is clear that the beam
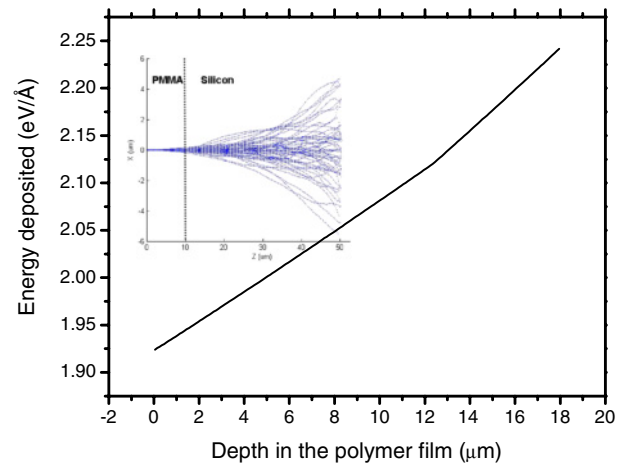

Fig. 2. (Color online) Energy deposition vs resist depth, using our Monte Carlo simulations for 2 MeV protons impinging into 18-µm-thick PMMA film on Si substrate.
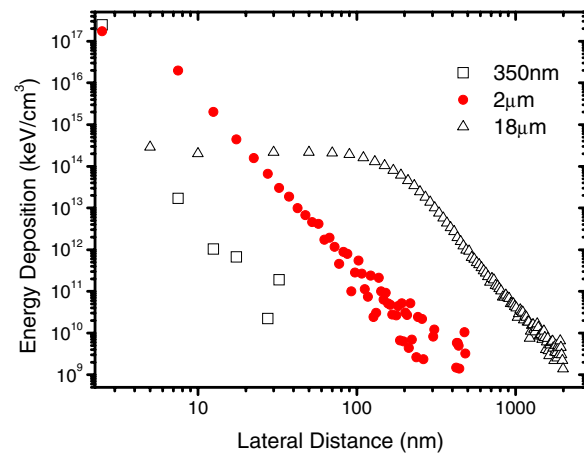

Fig. 3. (Color online) Energy deposition vs lateral dimension for various thicknesses of PMMA resist films (350 nm, 2 µm, and 18 µm) at the resist/Si interface. The beam broadening is very small despite of the very high film thicknesses.

broadening is very small regardless of the very high film thicknesses and is certainly considerably smaller compared with the broadening due to EBL. This limited beam broadening is the second advantage of PBW over EBL for thick resist film patterning. These two advantages make the PBW the ideal approach for maskless patterning of high-aspect-ratio structures limited only by the initial proton beam diameter and the ability of the resist material to withstand high-aspect-ratio structures.

The practical advantages of PBW over EBL are shown in the following figures. In Fig. 4, the resist profile after development in the case of a 350-nm-thick PMMA film on a Si substrate irradiated by a fine 2 MeV proton beam is shown. The layout consists of dense 100-nm-wide lines with a pitch of 150 nm. The simulated resist profile is vertical owing to limited scattering of the proton beam in the resist film. These results are in very good agreement with the results presented in the literature[13] for the same layout, film stack, and irradiation conditions.

In Fig. 5, the energy deposition and the resist profile (cross section) are shown for the case of a 2-µm-thick
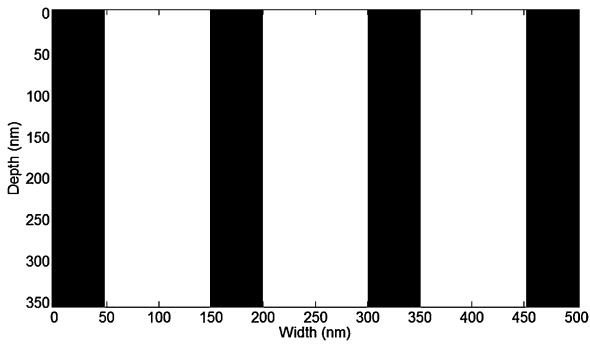
Fig. 4. Resist profile after PBW irradiation for 350-nm-thick film. The resist walls are vertical. These simulation results are in very good agreement with the experimental results obtained under the same irradiation conditions described in ref. 13.

TADEP film spin-coated onto a Si substrate. For the simulation of the development step, the threshold model, i.e., all the cells where the deposited energy exceeds a certain value do not dissolve during the development step owing to a high crosslinking density, is applied. Although this approach is considered to be simplified for the case of TADEP, it provides an indication of the expected results. Detailed simulation would require, among others, simulation of the PEB, *in situ* during the exposure and also on the hot plate, as well as the application of complex dissolution models leading to significant numerical problems arising from the resist thickness. The resist profile deviates slightly from vertical, as was expected from the energy deposition results shown in Fig. 3. However, this pattern broadening close to the resist/substrate interface is minimal compared with the one in the case of EBL.

These results are clear indications of the high potential of maskless patterning for sub-100 nm, dense high-aspect-ratio structures. The only limitations of those structures are unrelated to the physics of PBW but, in contrast, to the pattern collapse of very dense and very tall high-resolution structures.[14]

3.2 Experimental results

The TADEP samples spin-coating and PAB was carried at IMEL and then shipped to CIBA-NUS for further processing (exposure, PEB, development, electroplating). Although the sample underwent heavy temperature cycles, it was possible to process them without any additional treatment, which is evidence of the excellent stability and process latitude in terms of film quality and shelf life of the TADEP resist.

The spin coating was carried out using a Headway Research CR15 at 35000 rpm for 30 s for the 2-μm-thick sample from a 35% w/w ethyl lactate TADEP solution and at 3000 rpm for 30 s for the 12-μm-thick sample from a 45% w/w solution. PAB was performed on a levelled hotplate at 95 °C for 1 h for the thin film and for 2 h for the thick film followed by cooling down on the hotplate. PEB was performed at 110 °C for 2 and 8 min and development in TMAH for 2 and 8 min in light stirring mode.

In Fig. 6, features with a linewidth of 110 nm and thickness of 2 μm are shown. The layout consists of 2-pixel-wide lines with pitches of 1 μm and 4 μm and the calculated aspect ratio is 18. In Fig. 6(a), a low-magnifica-
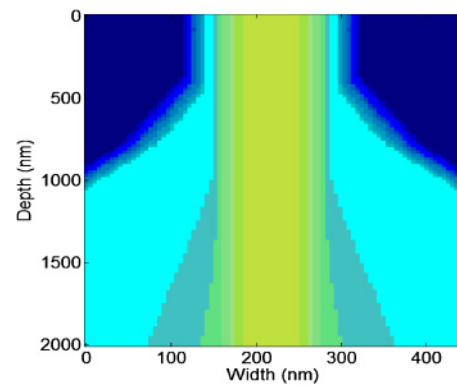

(a)
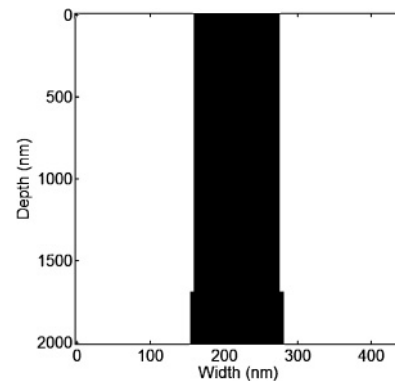
(b)

Fig. 5. (Color online) Resist profile after PBW irradiation for 2-μm-thick film. (a) Energy deposition profile (cross section) for a fine line with nominal width of 40 nm exposed by a beam with a diameter of 100 nm. (b) Resist profile after application of an energy deposition threshold value for development. The calculated linewidth is very close to the experimental one (Fig. 6).

tion top-view SEM image is presented, and in Fig. 6(b), a side view of the TADEP fine structure is shown. The measured linewidth is 110 nm in the *x*-direction and 220 nm in the *y*-direction. The beam diameter used was approximately 100×200 nm^2, very close to the linewidth resolved, showing that the TADEP resist has very limited acid diffusion, and the protons maintain an almost straight path in PBW. The observed corner rounding at the bottom of the cross pattern [Fig. 6(b)] could be attributed to the sum of parameters such as forward scattering range, the total exposure due to both vertical and horizontal lines, and the resist performance. In Fig. 7, features with a linewidth of 280 nm in the *x*-direction and an aspect ratio of 42 in a 12-μm-thick TADEP are shown. The resolved sidewalls are vertical and smooth proving that the proton beam is parallel and has an even energy deposition along its path.

4. Conclusions

Proton beam writing (PBW) is a valuable tool for the maskless patterning of high-aspect-ratio structures owing to the unique ability of protons to maintain a straight path over long distances. To explore the PBW patterning capabilities, a complete simulation tool was developed on the basis of a Monte Carlo module following the simulation procedure applied for electron beam lithography. Simulation results showed that the proton beam travels almost vertically with
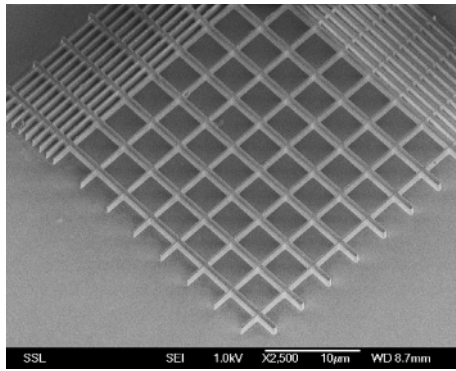
(a)
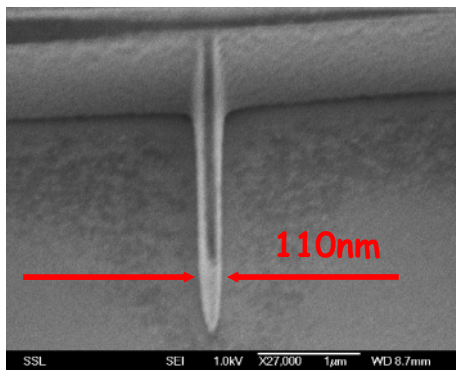
(b)

Fig. 6. (Color online) SEM images from the PBW on 2-μm-thick TADEP resist on Si. (a) Low-magnification top view of the irradiated area. (b) High-magnification side view of the fine patterns. Each line is a two-pixel pass line with beam step size of 10 nm. The pitch values were 1 μm and 4 μm and the calculated aspect ratio was 18.
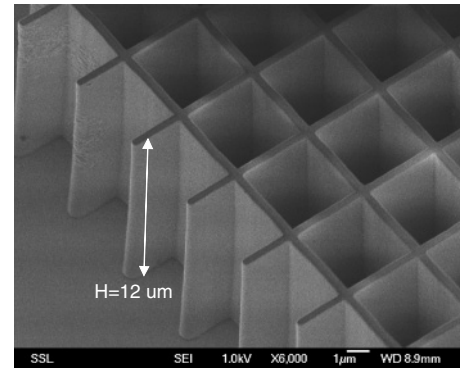

Fig. 7. Side-view SEM images from the PBW on 12-μm-thick TADEP resist on Si. Each line is a two-pixel pass line with beam step size of 10 nm. The pitch values were 1 μm and 4 μm and the calculated aspect ratio was 42.

limited beam broadening, which is a considerable advantage over EBL. For example, the forward scattering in 18-μm-thick films was estimated to be approximately 100 nm. These results prove the capability of PBW to produce very tall structures with almost vertical sidewalls, with the aspect ratio limited practically only by the resist performance and the beam diameter provided.

From an experimental point of view, the performance of PBW was explored and proved through the patterning of an aqueous base developable negative chemically amplified resist (TADEP). By employing PBW on 2.0-μm-thick TADEP, patterns with 110 nm linewidth and an aspect ratio of 18 were resolved.

1) E. W. Backer, W. Ehrfeld, D. Münchmeyer, H. Betz, A. Heuberger, S. Pongratz, W. Glashauser, H. J. Michel, and R. V. Siemens: Naturwissenschaften **69** (1982) 520.
2) R. A. Lawes: J. Micromech. Microeng. **15** (2005) 2198.
3) J. A. van Kan, P. G. Shao, K. Ansari, A. A. Bettiol, T. Osipowicz, and F. Watt: Microsyst. Technol. **13** (2007) 431.
4) J. A. van Kan, A. A. Bettiol, and F. Watt: Nano Lett. **6** (2006) 579.
5) I. Raptis, B. Nowotny, N. Glezos, M. Gentili, and G. Meneghini: Jpn. J. Appl. Phys. **39** (2000) 635.
6) J. Biersack and L. Haggmark: Nucl. Instrum. Methods **174** (1980) 257.
7) J. F. Ziegler, J. P. Biersack, and U. Littmark: *The Stopping and Ranges of Ions in Matter* (Pergamon Press, New York, 1985) Vol. 1.
8) International Commission on Radiation Units and Measurements: Stopping Powers and Ranges for Protons and Alpha Particles Report No. 49 (1993).
9) H. H. Andersen and J. F. Ziegler: *Stopping and Ranges of Ions in Matter* (Pergamon Press, New York, 1977) Vol. 3.
10) E. Everhart, G. Stone, and R. J. Carbone: Phys. Rev. **99** (1955) 1287.
11) F. Watt, J. A. van Kan, I. Rajta, A. A. Bettiol, T. F. Choo, M. B. H. Breese, and T. Osipowicz: Nucl. Instrum. Methods Phys. Res., Sect. B **210** (2003) 14.
12) M. Chatzichristidi, I. Rajta, Th. Speliotis, E. Valamontes, D. Goustouridis, P. Argitis, and I. Raptis: Microsyst. Technol. **14** (2008) 1423.
13) F. Watt, M. B. H. Breese, A. A. Bettiol, and J. A. van Kan: Mater. Today **10** (2007) No. 6, 20.
14) A. Jouve, J. Simon, A. Pikon, H. Solak, C. Vannuffel, and J.-H. Tortai: Proc. SPIE **6153** (2006) 61531C.